X-ray Crystal Structure of *Desulfovibrio vulgaris* Rubrerythrin with Zinc Substituted into the [Fe(SCys)$_4$] Site and Alternative Diiron Site Structures[†,‡]

Shi Jin,[§] Donald M. Kurtz, Jr.,*[,§] Zhi-Jie Liu,[||] John Rose,[||] and Bi-Cheng Wang[||]

Departments of Chemistry and Biochemistry and Molecular Biology, Center for Metalloenzyme Studies, and Georgia X-ray Crystallography Center, University of Georgia, Athens, Georgia 30602

Received September 8, 2003; Revised Manuscript Received January 8, 2004

ABSTRACT: The X-ray crystal structure of recombinant *Desulfovibrio vulgaris* rubrerythrin (Rbr) that was subjected to metal constitution first with zinc and then iron, yielding ZnS_4Rbr, is reported. A [Zn(SCys)$_4$] site with no iron and a diiron site with no appreciable zinc in ZnS_4Rbr were confirmed by analysis of the anomalous scattering data. Partial reduction of the diiron site occurred during the synchrotron X-ray irradiation at 95 K, resulting in two different diiron site structures in the ZnS_4Rbr crystal. These two structures can be classified as containing mixed-valent Fe1(III)(μ-OH^-)(μ-$GluCO_2^-$)$_2$Fe2(II) and Fe1(II)(μ-$GluCO_2^-$)$_2$Fe2(III)-OH^- cores. The data do not show any evidence for alternative positions of the protein or solvent ligands. The iron and ligand positions of the solvent-bridged site are close to those of the diferric site in all-iron Rbr. The diiron site with only the two carboxylato bridges differs by an ∼2 Å shift in the position of Fe1, which changes from six- to four-coordination. The Fe1- - -Fe2 distance (3.6 Å) in this latter site is significantly longer than that of the site with the additional solvent bridge (3.4 Å) but significantly shorter than that previously reported for the diferrous site (4.0 Å) in all-iron Rbr. The apparent redox-induced movement of Fe1 at 95 K in the ZnS_4Rbr crystal implies an extremely low activation barrier, which is consistent with the rapid (∼30 s^{-1}) room temperature turnover of the all-iron Rbr during its catalysis of two-electron reduction of hydrogen peroxide. ZnS_4Rbr does not show peroxidase activity, presumably because the [Zn(SCys)$_4$] site, unlike the [Fe(SCys)$_4$] site, cannot mediate electron transfer to the diiron site. One or both of the diiron site structures in the cryoreduced ZnS_4Rbr crystal are likely to represent that (those) of transient mixed-valent diiron site(s) that must occur upon return of the diferric to the diferrous oxidation level during peroxidase turnover.

Rubrerythrin (Rbr),[1] found in anaerobic and microaerophilic bacteria and archaea, is a homodimeric non-heme iron protein containing a non-sulfur, carboxylate-bridged diiron site and a rubredoxin-like [Fe(SCys)$_4$] site (*1*, *2*) within an ∼23 kDa protein subunit. The diiron site in the X-ray crystal structure of the recombinant oxidized all-ferric Rbr (Rbr_{ox}) from the sulfate-reducing bacteria *Desulfovibrio vulgaris* (cf. Figure 1) (*2*) contains one histidine and five carboxylate ligands. The side chain of a second histidine, His56, which had been predicted to be a ligand to the diiron site on the basis of sequence homologies to O_2-activating diiron proteins (*5*), was too distant to furnish a ligand to iron, but its Nϵ was within hydrogen-bonding distance of the carbonyl of C161 across the "head-to-tail" homodimer interface. C161 in turn furnished one of the thiolate ligands to the [Fe(SCys)$_4$] site. More recently, the X-ray crystal structure of the all-ferrous Rbr (Rbr_{red}) was reported (*4*). As shown schematically in Figure 1, the iron atom that was ligated to Glu97 in the Rbr_{ox} structure has moved ∼1.8 Å in Rbr_{red} to within ligating distance of His56 Nδ, which has replaced Glu97 as a ligand. The bidentate Glu20 carboxylate also followed the redox-induced movement of this iron. Other than these diiron site differences, the Rbr_{ox} and Rbr_{red} crystal structures are essentially superimposable. Due to its tendency toward disproportionation, no crystal structure is known for the mixed-valent [Fe(II,III)] diiron site of Rbr. The irons of this mixed-valent site are antiferromagnetically coupled, yielding an $S = {}^1/_2$ ground state with a characteristic EPR spectrum (*6*). ENDOR studies revealed that only one His ligates this mixed-valent diiron site and that the His ligates the ferrous iron (*7*). The magnitude of the magnetic coupling, $J \sim -8$ cm^{-1} (in the $-2JS_1 \cdot S_2$ formalism), strongly indicates a single atom, presumably hydroxo, bridge between the irons. The proposed structure of the mixed-valent diiron site that emerges from the cumulative spectroscopic studies is very similar to that of the all-ferric structure shown in Figure 1 except that His131 is ligated to Fe(II) rather than Fe(III) and the oxo is replaced by a hydroxo bridge (*7*). Mixed-metal

[†] This work was supported by NIH Grant GM40388 (D.M.K.).

[‡] Refined coordinates have been deposited in the Protein Data Bank. The accession number for the structure is 1QYB.

* To whom correspondence should be addressed at the Department of Chemistry. Phone: 706-542-2016. Fax: 706-542-9454. E-mail: kurtz@chem.uga.edu.

[§] Department of Chemistry and Center for Metalloenzyme Studies.

[||] Department of Biochemistry and Molecular Biology and Georgia X-ray Crystallography Center.

[1] Abbreviations: Rbr, rubrerythrin; Rbr_{ox}, all-ferric Rbr; Rbr_{red}, all-ferrous Rbr; ZnS_4Rbr, Rbr containing zinc in place of iron in the [Fe(SCys)$_4$] site; Tris, tris(hydroxylmethyl)aminomethane; EDTA, ethylenediaminetetracetic acid; GuHCl, guanidine hydrochloride; MOPS, 3-(*N*-morpholino)propanesulfonic acid; HEPES, *N*-(2-hydroxyethyl)-piperazine-*N*′-2-ethanesulfonic acid; DTPA, diethylenetriaminepentaacetic acid; PEG, poly(ethylene glycol); BDFM, Bijvoet difference Fourier map.

10.1021/bi0356193 CCC: $27.50
Published on Web 02/26/2004

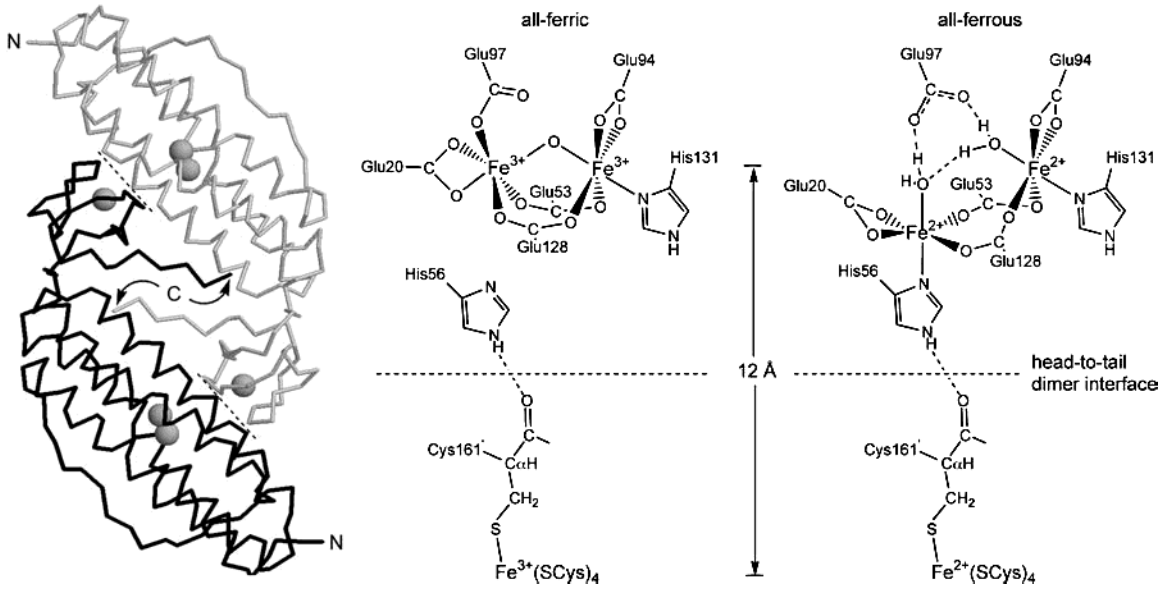

FIGURE 1: (Left) Protein backbone tracing of the *D. vulgaris* Rbr head-to-tail homodimer viewed along its 2-fold rotation axis drawn using RASMOL (*3*) and coordinates from PDB ID 1RYT (*2*). Amino (N) and carboxyl (C) termini are labeled, iron atoms are represented as spheres, and dashed lines indicate subunit interface regions between the [Fe(SCys)$_4$] and diiron sites. (Right) Schematic structure of the diiron sites and subunit interfaces of Rbr_{ox} (all-ferric) and Rbr_{red} (all-ferrous) structures (*4*).

Zn,Fe sites rather than diiron sites have also been reported in Rbr "as isolated" from *D. vulgaris* (*8*−*10*). The issue of metal site occupancy is addressed in the Discussion.

The function of Rbr has been controversial. *D. vulgaris* Rbr was reported to have ferroxidase activity (*11*), but the closely related protein, nigerythrin (*12*, *13*), from the same organism, does not show detectable ferroxidase activity (E. D. Coulter and D. M. Kurtz, Jr., unpublished results). Pyrophosphatase activity has been reported for *D. vulgaris* Rbr (*10*, *14*), but this activity could not be reproduced in two other laboratories (*5*, *12*) on either Rbr or nigerythrin, whether these proteins were recombinant or isolated directly from *D. vulgaris*. Both *D. vulgaris* Rbr and nigerythrin showed little or no superoxide dismutase or catalase activities using standard assays (*12*, *15*). Reduced *D. vulgaris* Rbr and nigerythrin are only sluggishly reactive with dioxygen; however, they both show high turnover rates as terminal components of NADH peroxidases in vitro (*16*, *17*). This last function of Rbr has been proposed as part of the oxidative stress protection system in some air-sensitive bacteria and archaea (*13*, *18*). Genetic evidence for an oxidative stress protection function of Rbr involving hydrogen peroxide is also available (*13*, *19*−*21*).

The aforementioned structural flexibility of the diiron site is likely to be an important feature of its unique reactivity and has been incorporated into a proposed mechanism for the Rbr_{red} reaction with hydrogen peroxide (*4*). Recombinant *D. vulgaris* Rbr constituted with first $Zn^{2+}{}_{aq}$ and then $Fe^{2+}{}_{aq}$ led to a protein named ZnS_4Rbr that, based on UV−vis absorption and EPR spectroscopies and metal analysis, contained diiron and, presumably, [Zn(SCys)$_4$] sites (*16*). ZnS_4Rbr showed no peroxidase or ferroxidase activities, supporting a reaction pathway in which external reducing equivalents enter through the [Fe(SCys)$_4$] site of Rbr_{ox} followed by internal electron transfer to the diiron site across the subunit interface, a distance of ∼12 Å (cf. Figure 1). Conversely, oxidation of Rbr_{red} by H_2O_2 was proposed to occur by direct reaction with the diferrous site, generating a transient Rbr species containing a diferric diiron site and a ferrous [Fe(SCys)$_4$] site, an oxidation level that would be mimicked in oxidized (i.e., diferric) ZnS_4Rbr. Verification of the metal site occupancies and structure of ZnS_4Rbr could thus help to clarify mechanistic questions about Rbr reactivity. Herewith is reported the X-ray crystal structure of *D. vulgaris* ZnS_4Rbr and anomalous scattering data in order to verify the metal site occupancies. A novel mixture of diiron site structures appears to be a result of cryoreduction in the synchrotron X-ray beam.

MATERIALS AND METHODS

ZnS_4Rbr Expression, Purification, and Crystallization. Recombinant *D. vulgaris* ZnS_4Rbr was expressed, metal-constituted, and purified using a procedure that was modified from that previously described (*16*). All of the following steps were carried out at room temperature, unless otherwise noted. Four 1 L cultures of *Escherichia coli* BL21(DE3)(pDK3-5) (*6*) were grown in M9 media with incubating/shaking at 37 °C and induced with 0.4 mM isopropyl β-D-thiogalactoside when the OD_{600} reached ∼0.8. The induced cultures were incubated at 37 °C for a further 5 h, after which time the cells were harvested by centrifugation. The cells were washed with 250 mL of 50 mM Tris-HCl and 2 mM EDTA, pH 8.0, then resuspended and incubated at 30 °C for 15 min in 120 mL of the same buffer to which was added 4 mL of 10 mg/mL lysozyme and 40 mL of 1% (v/v) Triton X-100, and then lysed by sonication. Unless otherwise noted, the buffer used in subsequent steps was 0.1 M Tris-HCl, pH 7.5. The ∼15 g wet weight of pellet obtained from centrifugation of the sonicated cells was resuspended in 12 mL of 4 M GuHCl in buffer and centrifuged at 30000*g* for 30 min. The supernatant was then transferred into a 250 mL Schlenk-type flask and subjected to several cycles of alternate degassing/N_2 gas flushing using a vacuum manifold. After each addition of (1) 40 μL of 2-mercaptoethanol and 5 mM sodium dithionite, (2) 130 μL of 0.14 M zinc sulfate in anaerobic buffer, and (3) 1.3 mL of 0.14 M ferrous

ammonium sulfate in anaerobic buffer, the solution in the flask was equilibrated with stirring for 0.5−1 h. The mixture was then diluted with stirring by dropwise addition of anaerobic buffer over the course of several hours to bring the total volume to ~80 mL. The diluted mixture was centrifuged as above to remove precipitate and then subjected to successive concentration and redilution cycles in an Amicon concentrator, as previously described for the iron incorporation procedure (*6*), except that 1 mM EDTA was added to the dilution buffer during the third round of dilution/concentration in order to aid in removal of any nonspecifically bound metal ions. The EDTA was removed by subsequent dilution/concentration cycles. The resulting pale yellow solution was treated with a small amount of H_2O_2 in order to obtain the homogeneous oxidized (diferric) diiron site. The resulting protein, referred to as ZnS_4Rbr_{ox}, was concentrated to 1.5 mM (homodimer) in 50 mM HEPES and 200 mM Na_2SO_4, pH 7.0, using a Centricon concentrator (5K mol wt cutoff) and stored at −80 °C. The yield was ~40 mg of ZnS_4Rbr. Crystallization was achieved using the hanging drop/vapor diffusion method. One and one-half microliters of the ZnS_4Rbr_{ox} solution, prepared as described above, was mixed with 1 μL of 27% (w/v) PEG1450 in 0.1 M Tris-HCl, pH 8.0, from the reservoir solution. Single crystals yellow in color with dimensions of ~0.5 × 0.2 × 0.2 mm were obtained in 2 days at room temperature. The crystals were rinsed with mineral oil as cryoprotectant and flash-cooled for data collection.

X-ray Diffraction Data Collection and Refinement. Data were collected on the IMCA-CAT insertion device beam line, using the ADSC Quantum 210 CCD detector mounted on a CrystalLogic goniostat (with ω and 2θ rotations) and equipped with the Oxford Cryosystems cryostream sample cooler at the Advanced Photon Source (Argonne National Laboratory). All data collection was performed on crystals cooled to 95 K. Two sets of data were collected on one ZnS_4Rbr crystal. The first data set was collected at a wavelength of 1.0 Å using 720 one-deg oscillations (resolution 1.75 Å). This was followed by collection of a second data set at 1.7 Å using 180 one-deg oscillations (resolution 2.05 Å). The total times of exposure of the crystal to the synchrotron beam were ~36 min at 1.0 Å and ~9 min at 1.7 Å. The programs DENSO and SCALEPACK (*22*) were used for data processing. Crystals of ZnS_4Rbr_{ox} were found to be isomorphous with those of published Rbr_{ox} and Rbr_{red} crystal structures (*2*, *4*), belonging to space group *I*222. Cell dimensions are listed in Table 1A. Each asymmetric unit contained one monomer. Since the two data sets were collected on the same crystal at different wavelengths, the data collected at 1.0 Å, which had the higher resolution, were used for refinement, using the difference Fourier analysis method. Omit maps ($F_o - F_c$), composite omit maps ($2F_o - F_c$) (*23*), and Bijvoet difference Fourier maps (ΔF; $\varphi + 90°$) (*24*, *25*) were calculated as described for data sets collected at both 1.0 and 1.7 Å. The Hendrickson−Lattman coefficients generated from each individual anomalous reflection file omitting Fe1, Fe2, and Zn3 and the same coordination file from the refined model with data collected at 1.0 Å were used for each map calculation with a resolution range below 3.0 Å. The model refinement and map calculation were performed in CNS 1.0 (*26*), and the model rebuilding against the map was carried out in O (*27*). The initial model was the all-iron Rbr_{ox} [PDB ID code 1LKM (*4*)] with all of the solvent molecules removed. About 8% of the reflection data were excluded for calculation of the R_{free} factor to monitor the refinement. The first round included rigid body refinement (data with resolution below 3.0 Å), energy minimization, and simulated annealing, which resulted in a decrease of R (R_{free}) from 0.388 (0.401) to 0.296 (0.327). The improved model was then used to calculate the composite omit map ($2F_o - F_c$), and both the model and the map were input into program O. A long bulky electron density overlapping the position of Fe1 in the initial model was found to have connections with the electron densities of both Oϵ1 of Glu97 and Nδ1 of His56. The Fe1 position was closer to Glu97 than to His56, because the electron density was not distributed evenly. Except for this feature, the overall electron density map at the diiron site fit the model very well. During the second round of refinement and energy minimization, grouped *B*-factor and individual *B*-factor refinement steps were sequentially carried out, and the first 138 waters with peak heights above 3σ were then picked by difference Fourier analysis, followed by another energy minimization refinement before map calculation. This second round of refinement decreased R (R_{free}) to 0.211 (0.240). Both the model and composite omit map were displayed in O. Although one end of the bulky electron

Table 1: Data Collection and Refinement Statistics

parameter	ZnS_4Rbr (1.0 Å)	ZnS_4Rbr (1.7 Å)
(A) Data Collection and Processing Statistics		
temperature (K)	95	95
unit cell dimensions (Å)		
a	48.0	48.0
b	80.2	80.2
c	101.0	101.3
maximum resolution (Å)	1.75	2.05
total reflections	286423	58521
unique reflections	20104	10507
completeness[a] (%)	99.3	83.7
R_{merge}[b] (%)	4.2 (14.5)[c]	5.8 (13.7)[c]
$\langle I\rangle/\langle\sigma(I)\rangle$	24.2	34.4
(B) Refinement Statistics		
resolution range for refinement	17.59−1.75	
R_{work} (%)	18.31	
R_{free}[d] (%)	21.42	
no. of water molecules	247	
no. of sulfate ions	1	
rmsd from ideality[e]		
bond lengths (Å)	0.005	
bond angles (deg)	1.0	
dihedral angles (deg)	19.2	
improper angles (deg)	0.75	
Wilson *B*-value (Å^2)	16.6	
mean *B*-value (Å^2)	21.0	
coordinate error[f] (Å)	0.18	
Ramachandran plot[g]		
residues in most favored regions (%)	94.0	
residues in additionally allowed regions (%)	6.0	
residues in generously allowed regions (%)	0	
residues in disallowed regions (%)	0	

[a] Values in parentheses correspond to the resolution shell. [b] $R_{merge} = \Sigma(|I - \langle I\rangle|)/\Sigma\langle I\rangle$. [c] Highest resolution shell. [d] Calculated with 8% of the complete data set excluded from refinement. [e] Stereochemical check was made using CNS. [f] Estimated coordinate error from the Luzatti plot. [g] Ramachandran plot was calculated using PROCHECK (*33*).

density occupied by Fe1 was connected with His56, similar to Fe1 in the diferrous site of Rbr_{red} (*4*), there was also electron density connecting Fe1 and Fe2 to each other at the position assigned to the oxo bridge in Rbr_{ox}. A water molecule was, therefore, centered into this electron density. Another 115 water molecules were selected during the third round of refinement, which decreased R (R_{free}) to 0.188 (0.221). A large electron density near Gln151 on the protein surface with tetrahedral geometry was fitted to a sulfate ion in O, since the protein buffer contained 200 mM Na_2SO_4 and no other added inorganic salts. Six disordered water molecules were found in the map and removed from the coordinate file in the final round of refinement. A total of 247 water molecules were included. Besides energy minimization, grouped *B*-factor, individual *B*-factor, and simulated annealing refinement, individual occupancy refinement for all water molecules and metal ions was carried out at the end, assuming the whole protein occupancy as 1. R (R_{free}) decreased to 0.183 (0.214). Data collection and refinement statistics are collected in Table 1.

Spectroscopy, Analyses, and Activity Assays. UV−vis absorption spectra were recorded on a Shimadzu UV-210PC spectrophotometer. EPR spectra were recorded on a Bruker ESP-300E spectrometer equipped with an ER-4116 dual-mode cavity and an Oxford Instruments ESR-9 flow cryostat. Metal/protein ratios were obtained by inductively coupled plasma-atomic emission metal analyses at the University of Georgia Chemical Analysis Facility and concomitant protein concentration determinations on the same samples using the Bio-Rad protein assay with recombinant *D. vulgaris* all-iron Rbr, isolated and purified as previously described (*6*), as standard (molar absorptivity $\epsilon_{494nm} = 10600$ M^{-1} cm^{-1} per Rbr homodimer). NADH peroxidase activities were determined similarly to the previously described procedure (*16*) in 1 cm path length cuvettes with 1 mL anaerobic solutions that typically contained initially 0.5 μM Rbr dimer, 0.5 μM BenC, 300 μM NADH, 350 μM H_2O_2, and 1 mM DTPA in 50 mM MOPS, pH 7.0.

RESULTS

ZnS_4Rbr_{ox} Characterization. The hydrogen peroxide treatment of the ZnS_4Rbr should have converted all iron centers to the ferric state as is the case for the all-iron Rbr (*16*, *17*). As shown in Figure 2, the UV−vis absorption spectrum of ZnS_4Rbr_{ox} features shoulders at ~330 and 480 nm and a peak at 370 nm that closely resemble the absorption spectrum of the diferric "chopped Rbr" (CRbr), an engineered form of *D. vulgaris* Rbr which lacks the rubredoxin-like domain (*6*). These absorption features are characteristic of a bent oxo-bridged diferric unit (*28*−*30*). A prominent resonance-enhanced Raman band at 520 cm^{-1} was also observed from ZnS_4Rbr_{ox} using 413 nm laser excitation (M. D. Clay, E. D. Coulter, M. K. Johnson, and D. M. Kurtz, Jr., unpublished results), which is similar to the 514 cm^{-1} $H_2{}^{18}O$-sensitive Raman band observed for the all-iron *D. vulgaris* Rbr with 406 nm laser excitation and assigned to the symmetric stretch of the oxo-bridged diferric unit (*31*). Any iron in the ferric [Fe(SCys)$_4$] site would have been manifested by its characteristic absorption features at ~370, 494, and ~570 nm, which dominate the visible absorption spectrum of all-ferric Rbr (cf. Figure 2, inset) (*6*). The 490 nm molar absorptivity

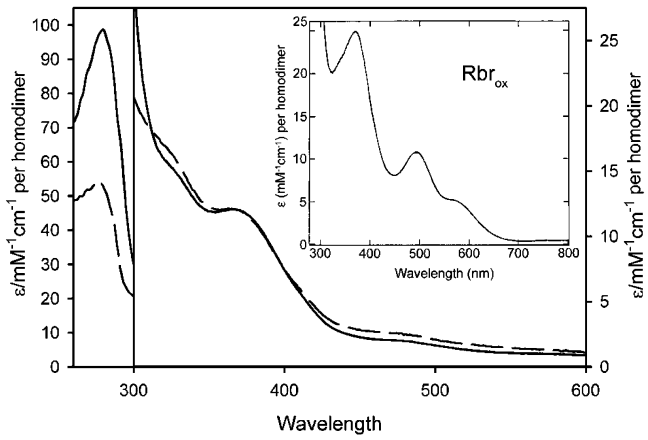

FIGURE 2: UV−vis absorption spectra of *D. vulgaris* ZnS_4Rbr_{ox} (solid trace) and CRbr (dashed trace) in 0.1 M Tris-HCl, pH 7.3. The absorbances of the ZnS_4Rbr_{ox} spectrum were multiplied by 1.5 to scale them to be equal to the extinction coefficient at 370 nm for CRbr (*6*) (actual $\epsilon_{370nm} = 7800$ M^{-1} cm^{-1} for ZnS_4Rbr_{ox}). The inset shows the absorption spectrum of recombinant Rbr_{ox} for comparison (*6*).

of ZnS_4Rbr_{ox} of 1300 M^{-1} cm^{-1} per protein dimer measured in this work is much less intense than the $\epsilon_{494nm} = 10600$ M^{-1} cm^{-1} (per protein dimer) for all-ferric Rbr (*6*). The absence of these intense absorption features is, therefore, consistent with a [Zn(II)(SCys)$_4$] site in ZnS_4Rbr_{ox}. The measured ϵ_{370nm} of 7800 M^{-1} cm^{-1} per protein dimer for ZnS_4Rbr is lower than the expected 12000 M^{-1} cm^{-1} (*6*) for full occupancy of the diiron sites. The measured iron content of as-isolated ZnS_4Rbr_{ox} was 3.4 Fe/protein dimer, which is also somewhat lower than the expected 4 Fe/dimer. Only a very weak mixed-valent diiron site EPR signal (g values of 1.99, 1.77, 1.63) was obtained for ZnS_4Rbr_{ox} [not shown (*32*)], when compared with those of recombinant all-iron Rbr_{ox} or CRbr (*6*) recorded under similar conditions, presumably because the ZnS_4Rbr_{ox} had been treated with H_2O_2. A weak $g = 4.3$ EPR signal, which could be due to either adventitious "junk" iron or a small portion of half-occupied diiron sites, also appeared. The measured zinc content of ZnS_4Rbr, 2.7 Zn/protein dimer, is somewhat higher than the 2 expected if zinc replaced iron only in the [Fe(SCys)$_4$] sites. The extra ~0.7 zinc is presumably adventitiously surface bound, since no zinc other than the two substituted into the [Fe(SCys)$_4$] site appeared in the X-ray crystal structure (see below). Confirming the previous observation (*16*), the ZnS_4Rbr_{ox} prepared as described here was found to have no detectable NADH peroxidase activity under conditions where the all-iron Rbr showed significant activity.

Crystal Structure of ZnS_4Rbr. The yellow color of the ZnS_4Rbr crystal became noticeably paler after exposure to the synchrotron X irradiation, which is consistent with partial reduction of the diiron sites during data collection. When the synchrotron X-ray-irradiated ZnS_4Rbr crystal was thawed in mineral oil, the pale yellow color became darker and close to the original color prior to exposure to the synchrotron irradiation within minutes of thawing, indicating reoxidation of the diiron site.

The X-ray diffraction data collected at 1.0 Å had a resolution of 1.75 Å, and the final model from refinement of the 1.0 Å data had good qualities, as shown in Table 1B,

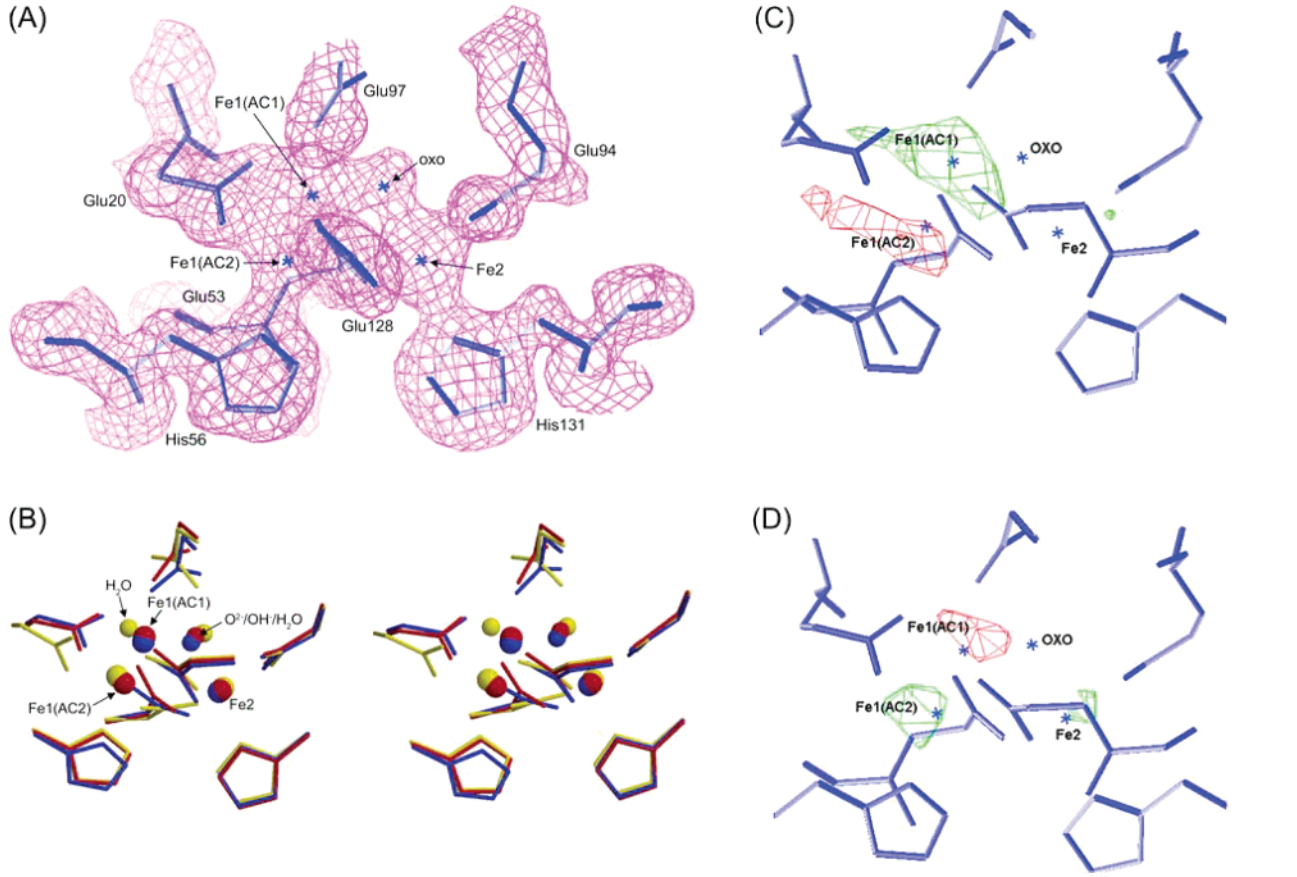

FIGURE 3: (A) Final model and composite omit map ($2F_o - F_c$) contoured at 1.0σ at the diiron site of the *D. vulgaris* ZnS_4Rbr crystal structure. Glu128 is in the foreground, and Glu53 is in the background. Stars indicate positions of iron atoms and the solvent ligand modeled as an oxo. (B) Stereoview of the diiron sites resulting from superposition of the protein subunits in the *D. vulgaris* ZnS_4Rbr (red), all-iron Rbr_{ox} (blue), and all-iron Rbr_{red} (yellow) crystal structures. The smaller spheres represent solvent ligands, and the larger spheres represent irons. (C) $F_o(ZnS_4Rbr) - F_o$(all-iron Rbr_{ox}) omit maps contoured at +3.0σ (in red) and −3.0σ (in green). (D) $F_o(ZnS_4Rbr) - F_o$(all-iron Rbr_{red}) omit maps contoured at +6.0σ (in red) and −6.0σ (in green). For both (C) and (D) The Fe1(AC1), Fe1(AC2), Fe2, and solvent (oxo) in ZnS_4Rbr (1.0 Å) were omitted from the calculation of the omit maps, which are superimposed on the final model at the diiron site of ZnS_4Rbr (1.0 Å) (with stars indicating positions of metals and oxo).

with low rmsd's from ideal bond lengths, angles, and torsion angles, as well as reasonable *B*-value and coordinate errors. Ramachandran plots using PROCHECK (*33*) showed that the majority of the residues in the model are in the most favored regions, other residues are in additionally allowed regions, and no residues are in generously allowed or disallowed regions. The ZnS_4Rbr (1.0 Å) crystal structure is very similar to that of all-iron Rbr_{ox} [PDB ID 1LKM (*4*)] with an rmsd of 0.63 Å over all atoms. As in all other reported *D. vulgaris* Rbr crystal structures, the ZnS_4Rbr crystallized as a tetramer, with protein subunits related to each other as "head-to-head" and "head-to-tail dimers (*2*). Nevertheless, as for Rbr_{ox}, only the ZnS_4Rbr dimer is detected in solution. The major differences from the Rbr_{ox} crystal structure are the zinc substitution at the [Fe(SCys)$_4$] site and the position of Fe1 at the diiron site in ZnS_4Rbr.

The iron and zinc ions can be differentiated by their distinctive anomalous scattering properties at the two X-ray wavelengths used in this study. The structures of the metal sites are first described, identifying the metals as those determined from the subsequently described analysis of the anomalous scattering data. The composite omit ($2F_o - F_c$) map shown in Figure 3A displays the expected electron density at Fe2 connected to Glu53, Glu94, Glu128, His131, and solvent (oxo) as in the all-iron Rbr_{ox} and Rbr_{red} crystal structures. The electron density at Fe1 connecting Glu97 and His56 (cf. Figure 3A), on the other hand, has two centers, which we label Fe1(AC1) and Fe1(AC2). The locations of these two centers were confirmed by the annealed ($F_o - F_c$) electron density map, omitting Fe1, Fe2, Zn3, solvent bridge (oxo), and the surrounding residues within 3.5 Å from the omitted atoms, as shown in Figure 4A. The 1.9 Å separation between the AC1 and AC2 positions of Fe1 is too close for simultaneous occupancy of these two positions by a divalent or trivalent metal ion; i.e., a trinuclear metal site is not a physically reasonable interpretation of the electron density map. On the basis of the peak height in the $F_o - F_c$ omit map, the electron density attributed to solvent (oxo) is connected to both Fe1(AC1) and Fe2 but is not connected to Fe1(AC2). The superposed diiron site structures in Figure 3B as well as the $F_o(ZnS_4Rbr) - F_o$(all-iron Rbr_{ox}) and $F_o(ZnS_4Rbr) - F_o$(all-iron Rbr_{red}) omit maps (cf. Figure 3C,D) also show that the alternative positions, AC1 and AC2, of Fe1 are close to those in all-iron Rbr_{ox} and all-iron Rbr_{red}, respectively. The latter two maps essentially rule out the possibility that the alternative positions of Fe1 in ZnS_4Rbr are occupied by tightly bound solvent rather than metal atoms. Alternative positions are not apparent for any of the diiron site ligands (or for Fe2) in the ZnS_4Rbr crystal structure.

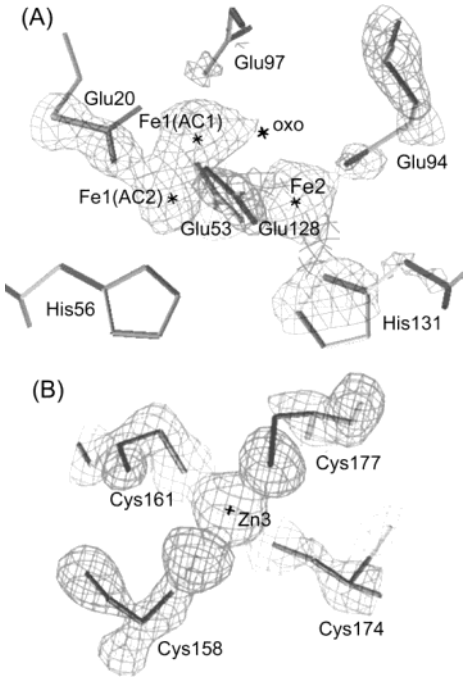

FIGURE 4: Final model and annealed omit map ($F_o - F_c$) contoured at 3.0σ for (A) the diiron site and (B) the [Zn(SCys)$_4$] site of the *D. vulgaris* ZnS$_4$Rbr crystal structure. Surrounding atoms within 3.5 Å of Fe1, Fe2, Zn3, and solvent (oxo) were omitted. Stars indicate positions of metal atoms and oxo.

Table 2 compares interatomic distances for the diiron sites of ZnS$_4$Rbr, all-iron Rbr$_{ox}$, and all-iron Rbr$_{red}$, and the diiron site structures in these three proteins are superimposed in Figure 3B. The Fe1(AC1)- - -Fe2 distance (3.4 Å) in the ZnS$_4$Rbr structure is the same as the Fe1- - -Fe2 distance (3.3 Å) in all-iron Rbr$_{ox}$ within experimental error. The side chains of Glu94 and His131, which exclusively ligate Fe2, show no significant changes in the ZnS$_4$Rbr structure, compared to those of all-iron Rbr$_{ox}$ and Rbr$_{red}$. Similarly, the positions of the two bridging carboxylates from Glu53 and Glu128 in the ZnS$_4$Rbr structure are close to those in all-iron Rbr$_{ox}$. The positions of the carboxylate planes of the Fe1 ligands, Glu20 and Glu97, in ZnS$_4$Rbr are also closer to those in all-iron Rbr$_{ox}$ than all-iron Rbr$_{red}$. The Glu20 appears to be bidentate to Fe1(AC1), as in Rbr$_{ox}$, but monodentate (via Oϵ2) to Fe1(AC2), unlike Fe1 in Rbr$_{red}$. A nonligating solvent molecule (not shown) is within hydrogen-bonding distance of Glu20 Oϵ1 and may help to compensate for the change from bidentate to monodentate ligation to Fe1. A solvent molecule is present in a similar position in both Rbr$_{ox}$ and Rbr$_{red}$ structures. The position of the imidazole ring of His56 in ZnS$_4$Rbr is slightly closer to that in Rbr$_{red}$ than Rbr$_{ox}$, although the difference is not significant. The distance between the His56 Nϵ and Cys161′ carbonyl oxygen in ZnS$_4$Rbr is identical to that in Rbr$_{red}$ (2.8 Å); i.e., this intersubunit hydrogen bond (cf. Figure 1) is well maintained in ZnS$_4$Rbr. If Fe1(AC2) is disregarded, the diiron site structure of ZnS$_4$Rbr is very similar to that of Rbr$_{ox}$ with the same six side chain and solvent ligands to both Fe1(AC1) and Fe2. As for Rbr$_{ox}$, His56 Nδ1 is too far away (~4.0 Å) to be a ligand to Fe1(AC1) in ZnS$_4$Rbr. We presume that Nδ of this nonligating His56 is not protonated because the ZnS$_4$Rbr was crystallized well above pH 7 and because hydrogen-bonding interactions to a putative His56 NδH$^+$ are not apparent in the crystal structure. (This same presumption is implicit in the schematic all-ferric Rbr$_{ox}$ structure shown in Figure 1.) While the solvent bridge between Fe1(AC1) and Fe2 was modeled as oxo, its protonation state is difficult to discern from the structural data. As reported for previous *D. vulgaris* Rbr structures (*2*, *4*), several water molecules were observed to occupy the "canyon" leading from the diiron site to the surface of the protein in the ZnS$_4$Rbr structure. None of these observable waters, however, are within hydrogen-bonding distance of the solvent bridge between Fe1 and Fe2 in the ZnS$_4$Rbr structure; the closest nonligating atom to the diiron solvent bridge visible in the structure is the carbonyl oxygen of the monodentate Glu97 carboxylate at a distance of 3.1 Å. The alternative location of Fe1 at AC2 is well beyond bonding distance of Glu97 but well within bonding distance of His56 Nδ1, as is Fe1 in all-iron Rbr$_{red}$ (cf. Table 2). The Fe1(AC2)- - -Fe2 distance (3.6 Å), however, is significantly shorter than the Fe1- - -Fe2 distance in all-iron Rbr$_{red}$ (4.0 Å). The solvent ligand to Fe2 is terminal in this alternative diiron site structure and is 3.0 Å from what had been the ligating carboxyl oxygen of Glu97, which could, therefore, form a hydrogen bond to the solvent ligand. The most striking difference in this alternative diiron site structure compared to those of either Rbr$_{ox}$ or Rbr$_{red}$ is that only four atoms, all from protein side chains, are within bonding distance of Fe1(AC2) (cf. Table 2), resulting in an approximately tetrahedral coordination sphere. The [Zn(SCys)$_4$]

Table 2: Interatomic Distances for Metal Sites in the Crystal Structure of *D. vulgaris* ZnS$_4$Rbr, All-Iron Rbr$_{ox}$, and All-Iron Rbr$_{red}$[a]

atoms	ZnS$_4$Rbr	Rbr$_{ox}$[b,c]	Rbr$_{red}$[b,c]
Fe1(AC1)−O(oxo/solvent)	2.0	1.8	
Fe1(AC1)−Glu20 OE1	2.0	2.1	
Fe1(AC1)−Glu20 OE2	2.6	2.3	
Fe1(AC1)−Glu53 OE1	2.2	2.2	
Fe1(AC1)−Glu128 OE2	2.0	2.0	
Fe1(AC1)−Glu97 OE1	2.3	2.1	
Fe1(AC1)−His56 ND1	(4.0)	(4.2)	
Fe1(AC2)−oxo/solvent	(3.3)		2.2
Fe1(AC2)−Glu20 OE1	(2.9)		2.2
Fe1(AC2)−Glu20 OE2	2.1		2.3
Fe1(AC2)−Glu53 OE1	2.4		2.1
Fe1(AC2)−Glu128 OE2	2.2		2.1
Fe1(AC2)−Glu97 OE1	(4.0)		(4.6)
Fe1(AC2)−His56 ND1	2.2		2.3
Fe2−O(oxo/solvent)	2.2	2.1	2.2
Fe2−Glu94 OE1	2.3	2.2	2.2
Fe2−Glu94 OE2	2.3	2.2	2.3
Fe2−Glu53 OE2	2.2	2.0	2.1
Fe2−Glu128 OE1	2.2	2.1	2.1
Fe2−His131 ND1	2.2	2.2	2.2
Zn3/Fe3−Cys158 SG	2.3	2.4	2.3
Zn3/Fe3−Cys161 SG	2.3	2.3	2.3
Zn3/Fe3−Cys174 SG	2.3	2.3	2.3
Zn3/Fe3−Cys177 SG	2.3	2.3	2.3
avg Zn3−Cys SG	2.3	2.3	2.3
Fe1(AC1)---Fe2	(3.4)	(3.3)	
Fe1(AC1)---Zn3/Fe3	(12.6)	(12.4)	
Fe1(AC2)---Fe2	(3.6)		(4.0)
Fe1(AC2)---Zn3/Fe3	(10.8)		(11.0)
Fe2---Zn3/Fe3	(12.0)	(12.0)	(12.2)
Fe1(AC1)---Fe1(AC2)	(1.9)		

[a] Distances in parentheses are nonbonding. [b] Data from Jin et al. (*4*). [c] The distances from Fe1 in Rbr$_{ox}$ and Rbr$_{red}$ are listed across from those of the corresponding distances from Fe1(AC1) and Fe1(AC2), respectively.

Table 3: Peak Heights (σ) of the Metals in the $F_o - F_c$ Annealed Omit Maps (AOM) and Bijvoet Difference Fourier Maps (BDFM) from the 1.0 and 1.7 Å Data for ZnS_4Rbr

	1.0 Å				1.7 Å		
	Fe1(AC1)[a]	Fe1(AC2)[a]	Fe2	Zn3	Fe1	Fe2	Zn3
AOM	11.5	7.6	17.1	37.6			
BDFM							
3.0 Å res[b]	14.2[d]		13.3	42.6	23.7[d]	20.4	8.6
2.05 Å res[c]	19.0[d]		23.8	73.7	24.1[d]	24.1	8.6

[a] AC1 and AC2 represent the two centers at Fe1. [b] Peak heights calculated using a resolution range below 3.0 Å. [c] Peak heights calculated using a resolution range below 2.05 Å. [d] Including both AC1 and AC2 centers.

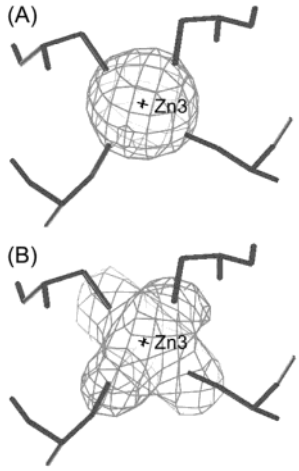

FIGURE 5: Final model and Bijvoet difference Fourier maps contoured at 3σ at the [Zn(SCys)$_4$] sites of ZnS_4Rbr from the (A) 1.0 Å and (B) 1.7 Å data with Fe1, Fe2, and Zn3 omitted. Maps were calculated using a resolution range below 3.0 Å. Stars indicate positions of zinc atoms.

center in ZnS_4Rbr (cf. Figure 4B and Table 2) is essentially isostructural with the [Fe(SCys)$_4$] center in Rbr_{ox}. The rmsd of the ZnS_4Rbr crystal structure vs the all-iron Rbr_{ox} structure for the four cysteine residues (Cys158, Cys161, Cys174, Cys177) is only 0.05 Å.

Anomalous Scattering. Table 3 tabulates the anomalous scattering data for the ZnS_4Rbr crystal obtained at the two wavelengths, 1.0 and 1.7 Å. For the 1.0 Å data the peak height of Zn3 (37.6σ) in the ($F_o - F_c$) annealed omit map is much higher than those of Fe1 [11.5σ (AC1), 7.6σ (AC2)] and Fe2 (17.1σ), as expected if zinc occupies the Zn3 site and iron occupies the Fe1 and Fe2 sites. Bijvoet difference Fourier maps (BDFMs) (*24*) can distinguish zinc from iron according to their respective anomalous scattering coefficients at each of the two wavelengths (1.0 or 1.7 Å). The iron anomalous scattering coefficient, f'' at 1.7 Å is ~4.6 times that of zinc, whereas at 1.0 Å, f'' for iron is only ~61% that of zinc (*25*). A comparison of the relative peak heights for Fe1, Fe2, and Zn3 in the two BDFMs of ZnS_4Rbr (Table 3) shows that Zn3 has the most intense anomalous scattering at 1.0 Å but the weakest anomalous scattering at 1.7 Å. Figure 5 shows the BDFMs for the Zn3 site from data obtained at each of the two wavelengths. Four zinc−sulfur bonds appear in the BDFM from the 1.7 Å data (Figure 5B), whereas these connections are not detectable in the corresponding map from the 1.0 Å data, where essentially only the zinc is detectable (Figure 5A). The BDFM from the 1.7 Å data for the Zn3 site is consistent with the similar anomalous scattering coefficients, f'', of sulfur (0.67) and zinc (0.81) at 1.7 Å, both of which are relatively weak compared to f'' for iron (3.75) at this wavelength (*25*). Conversely, the absence of significant scattering intensity from sulfur and relatively intense scattering for Zn3 in the 1.0 Å BDFM is consistent with the small f'' for sulfur (0.24) and large f'' for zinc (2.55) at 1.0 Å. From this analysis of the BDFMs for the Zn3 site together with the UV−vis absorption spectra discussed above, we conclude that the iron in the Fe(SCys)$_4$ site of Rbr has been fully substituted by Zn^{2+} in ZnS_4Rbr. BDFMs from both the 1.0 and 1.7 Å data for the diiron site that were calculated using a resolution range of 2.05 Å or lower (the maximum resolution possible for the 1.7 Å data) are shown in Figure 6. The two Fe1 centers, AC1 and AC2, in the final model could not be resolved in the BDFMs, and therefore, only one peak height for Fe1 (at the positions indicated by the arrows in Figure 6) is reported in Table 3. Nevertheless, both the contours and the intensities are very similar at Fe1(AC1), Fe1(AC2), and Fe2 within each of the two BDFMs and show the trends relative to those of the Zn3 sites expected for iron occupancy of the Fe1 and Fe2 centers. These BDFMs and the peak heights listed in Table 3 thus rule out the possibility that the Fe1(AC1), Fe1(AC2), or Fe2 centers have any significant

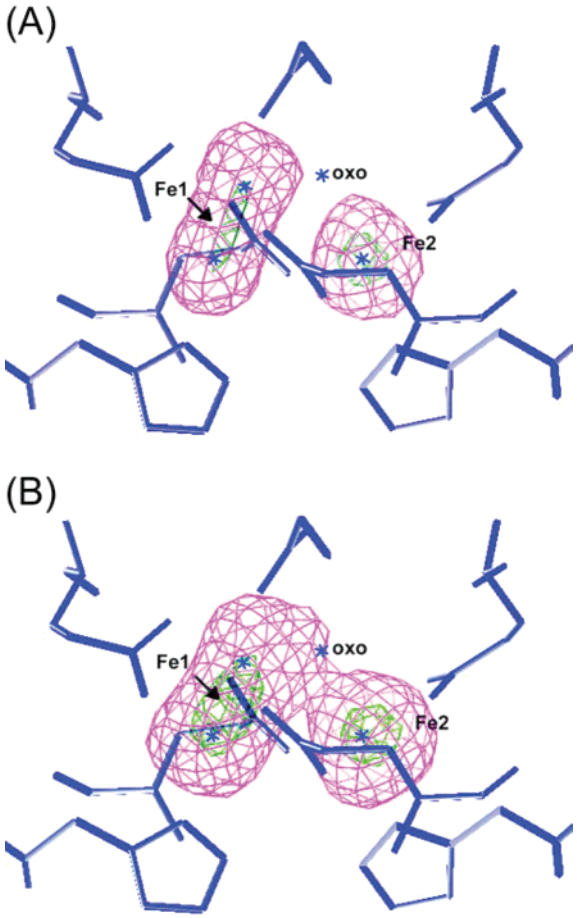

FIGURE 6: Final model and Bijvoet difference Fourier map contoured at 3σ (magenta) and 16σ (green) for the diiron sites of ZnS_4Rbr from the (A) 1.0 Å and (B) 1.7 Å data with Fe1, Fe2, and Zn3 omitted. Maps were calculated using a resolution range below 2.05 Å. Stars indicate positions of iron atoms and solvent (oxo), and arrows indicate centroids of electron density at the Fe1 site.

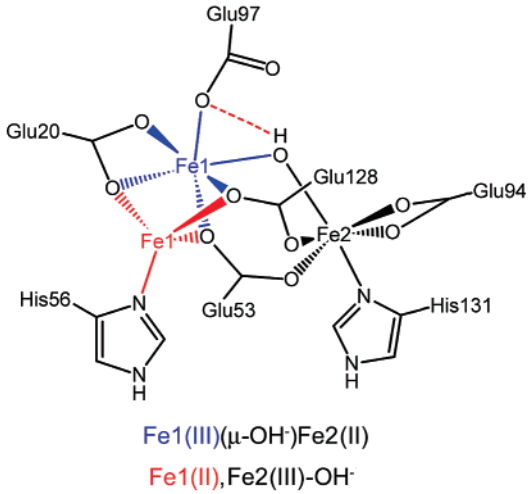

FIGURE 7: Schematic drawing of the diiron site structures in the *D. vulgaris* ZnS$_4$Rbr crystal and proposed assignments of iron oxidation states resulting from cryoreduction. The irons at the alternative Fe1 positions, AC1 and AC2, and their bonds to the surrounding ligands are highlighted in blue and red, respectively.

occupancy by zinc.[2] In the ($F_o - F_c$) annealed omit map (cf. Figure 4A) the sum of the peak heights of Fe1(AC1) and Fe1(AC2) (19.1σ) is approximately equal to that of Fe2 (17.1σ) (cf. Table 3), consistent with similar iron occupancies at Fe1 and Fe2. The relative peak heights at the two Fe1 positions may indicate somewhat more iron at AC1 than at AC2.

DISCUSSION

Two distinct diiron site structures emerge from the cumulative analysis of the data on *D. vulgaris* ZnS$_4$Rbr. Figure 7 contains a schematic diagram of these two structures, which we label Fe1(AC1),Fe2 and Fe1(AC2),Fe2. These two structures differ essentially only in the position of Fe1. The [Zn(II)(SCys)$_4$] site in ZnS$_4$Rbr is essentially isostructural with those of the [Fe(II/III)(SCys)$_4$] sites in the all-iron Rbr$_{ox/red}$ structures. The homologous iron in rubredoxin can also be replaced by zinc, leading to a protein that is isostructural with the native iron rubredoxin but with slightly longer metal−sulfur bonds (*34*). The N−H- - -S hydrogen-bonding pattern to the cysteine ligands is unaltered from that of the corresponding all-iron proteins for both ZnS$_4$Rbr and zinc-substituted rubredoxin. Thus, substitution of iron by zinc does not significantly alter the structures of [Fe(SCys)$_4$]-containing sites in proteins. Furthermore, the absorption spectra (cf. Figure 2) and resonance Raman spectra show that the diferric site structure in ZnS$_4$Rbr, with its very stable oxo bridge, closely resembles that in Rbr$_{ox}$ (cf. Figure 1). Therefore, the possibility that the alternative diiron site structures in ZnS$_4$Rbr represent oxo-bridged and nonsolvent-bridged diferric sites and that the latter structure was induced by the substitution of a [Zn(II)(SCys)$_4$] for an [Fe(III)(SCys)$_4$] site seems highly unlikely. The possibility that iron at Fe1 was partially reduced and shifted from AC1 to AC2 prior to freezing of the ZnS$_4$Rbr crystal also seems unlikely given the hydrogen peroxide treatment of the ZnS$_4$Rbr preparation prior to crystallization, which was carried out aerobically and with no added reducing agents, and the fact that such reduction and shifting of Fe1 were not observed in similarly crystallized and frozen all-iron Rbr$_{ox}$ crystals that were exposed to conventional rather than synchrotron X-ray sources (*4*). The fading of the color of the frozen ZnS$_4$Rbr crystal when subjected to synchrotron irradiation and the reintensification of the color upon thawing indicate that the alternative diiron site structures instead arose from cryoreduction of the diiron sites.

The Fe1(AC1),Fe2 site structure is very similar to that in all-iron Rbr$_{ox}$ (cf. Figure 1). The Fe1(AC2),Fe2 site structure, on the other hand, closely resembles that identified as a Zn,Fe site in Rbr as isolated from *D. vulgaris* (PDB ID 1DVB) (*8*, *9*). Anomalous scattering data on the as-isolated Rbr crystal obtained at a single wavelength were consistent with zinc rather than iron occupying the position corresponding to Fe1(AC2) and with no metal occupying the position corresponding to Fe1(AC1). The anomalous scattering data obtained at two different wavelengths on our ZnS$_4$Rbr crystal, however, rule out the possibility that Fe1(AC2) contains a significant proportion of zinc[2] and, in fact, show that both Fe1(AC1),Fe2 and Fe1(AC2),Fe2 are predominantly diiron sites. The Fe1(AC2),Fe2 structure can, thus, apparently be attained by a diiron site as well as a Zn,Fe site, and this structure may be favored when a divalent metal occupies the Fe1 center and a trivalent metal occupies the Fe2 center. The same workers who reported the Zn,Fe site in the crystal structure had earlier reported spectroscopic results on as-isolated *D. vulgaris* Rbr which clearly showed an oxo-bridged diferric site and no evidence for a Zn,Fe site (*1*, *31*). An independent group also clearly demonstrated by EPR spectroscopy the presence of a mixed-valent diiron site in Rbr as isolated from *D. vulgaris* (*12*). In our experience zinc in variable and nonstoichiometric quantities is nearly always detected by metal analyses of *D. vulgaris* Rbr, whether recombinant and constituted only with iron or isolated directly from *D. vulgaris*. Therefore, the possibility that the native Rbr produced in *D. vulgaris* contains a diiron site and that zinc displaced iron from the Fe1 center during either isolation or crystallization seems more likely to us than the opposite scenario implied in the reports of the as-isolated Rbr crystal structures (*8*−*10*). We have, in fact, shown by anomalous scattering studies analogous to those described here that zinc can partially displace iron from *both* Fe1 and Fe2 positions of the diiron site simply by incubating recombinant all-iron *D. vulgaris* Rbr with excess zinc sulfate (*35*).

The position and ligation pattern of Fe1(AC1) with Glu97 but not His56 furnishing a ligand is nearly identical to that of the highly negatively charged, all-oxygen coordination sphere of the ferric Fe1 of Rbr$_{ox}$ (cf. Figure 1). Fe1(AC1) also has the solvent (oxo or hydroxo) bridging ligand found for the ferric Fe1 of Rbr$_{ox}$. The assignment of a ferric oxidation state to iron at Fe1(AC1) in ZnS$_4$Rbr, thus, seems straightforward. The iron at Fe1(AC2), on the other hand, has likely been reduced by the synchrotron X irradiation. While none of the other Rbr crystal structures in the Protein Data Bank used data obtained from a synchrotron source, reduction of iron by such sources has been observed in other non-heme diiron proteins (*36*−*40*), and these other diiron sites have significantly lower reduction potentials than those of Rbr (*6*, *12*). Similarly, while the four-coordination at

[2] Our data do not rule out the possibility that a very minor proportion of the metal at Fe1(AC2) is zinc.

Fe1(AC2) with carboxylate oxygen and histidine nitrogen ligands has not been reported previously for iron in Rbr, it has been observed in mixed-valent or diferrous sites of other non-heme diiron proteins (*30*, *41*); i.e., four-coordination appears to be characteristic of ferrous but not ferric centers in these proteins. In fact, we are unaware of any synthetic tetrahedral, four-coordinate Fe(III) complex having an N,3O coordination sphere resembling that of Fe1(AC2). The iron at Fe1(AC2) in ZnS_4Rbr is, thus, almost certainly ferrous. The coordination structure at Fe2 in ZnS_4Rbr does not readily distinguish ferric from ferrous oxidation states. The ferric and ferrous Fe2 sites of all-iron Rbr_{ox} and Rbr_{red}, respectively (*4*), have coordination spheres that are very similar to each other, being distinguished only by their bridging and terminal solvent ligands, respectively. The average of the Fe2−ligand atom distances is slightly longer in ZnS_4Rbr than in Rbr_{ox} (cf. Table 2), consistent with some proportion of ferrous iron at Fe2 in the ZnS_4Rbr structure. We, therefore, propose that exposure of the ZnS_4Rbr crystal to synchrotron X-ray irradiation at 95 K resulted in rapid reduction of either Fe1 or Fe2, but not both, at each diiron site and that reduction of Fe1 resulted in its movement from position AC1 to AC2 and breakage of the solvent bridge. Cryoreduction of ZnS_4Rbr would, thus, result in two mixed-valent diiron sites differing by a bridging vs terminal solvent ligand, six- vs four-coordinate Fe1, and reversals of their iron oxidation states, viz., Fe1(AC1),Fe2 having an Fe1(III)(μ-OH^-)(μ-RCO_2^-)$_2$Fe2(II) core and Fe1(AC2),Fe2 having an Fe1(II)(μ-RCO_2^-)$_2$Fe2(III)-OH^- core (cf. Figure 7). If one includes the Glu97 carboxylate, both mixed-valent sites would have the same overall net charge (−1). Ligand rearrangements necessary to attain the structure of the diferrous site in all-iron Rbr_{red} (cf. Figure 1), including addition of a solvent ligand to Fe1, translation of the bidentate Glu20 side chain, rotation of the Glu97 and Glu53 carboxylates, and, presumably, protonation of the hydroxo ligand to Fe2, are all likely to be inhibited at 95 K. This inhibition may have prevented cryoreduction of the diiron sites in the ZnS_4Rbr crystal to below the mixed-valent oxidation level. The reintensification of the color of the irradiated ZnS_4Rbr crystal upon thawing could have been due to oxidation by dioxygen and to disproportionation of mixed-valent diiron sites formed during cryoreduction (*6*).

On the basis of ENDOR spectroscopy of the $S = {}^1/_2$ EPR signal and the magnitude of the antiferromagnetic coupling between the irons, a structure of the mixed-valent diiron site in all-iron Rbr was proposed that is essentially identical to the Fe1(AC1),Fe2 structure in ZnS_4Rbr, including the Fe1(III)(μ-OH^-)(μ-RCO_2^-)$_2$Fe2(II) core (*7*). Notably, the $S = {}^1/_2$ EPR signal of the all-iron Rbr intensified upon cryoreduction by γ-irradiation at 77 K, implying that formation of the mixed-valent from the diferric site and proton transfer to the oxo bridge of Rbr_{ox} (cf. Figure 1) can both occur at this low temperature (*7*). We know of no examples of a mixed-valent Fe(II),Fe(III) complex having only two carboxylato bridges, i.e., having the bridging ligand structure of Fe1(AC2),Fe2 in ZnS_4Rbr. Given the four- and six-coordination of Fe1(AC2) and Fe2, respectively, a mixed-valent Fe1(AC2),Fe2 diiron site would almost certainly be valence-localized, and the magnetic superexchange coupling mediated by the two carboxylato bridges is expected to be much weaker than that mediated by a hydroxo bridge (*30*). Such weak superexchange coupling in a mixed-valent diiron(II,III) site would result in a very anisotropic *g* tensor and make its EPR spectrum difficult to observe (*7*, *42*); i.e., the $S = {}^1/_2$ EPR signal observed from Rbr is much more likely to be due to the hydroxo-bridged mixed-valent site.

Although structural plasticity is a characteristic feature of diferric/diferrous redox interconversions of non-heme diiron sites in other proteins (*30*, *40*, *41*), Rbr is unique in that this plasticity involves a nearly 2 Å movement of one of the irons accompanied by ligand exchange between histidine and carboxylate side chains (*4*). Perhaps the most remarkable result of the studies reported here is that the redox-induced ∼2 Å movement and change from six- to four-coordination of the Fe1 iron in the ZnS_4Rbr crystal must have occurred at 95 K. The low-activation barrier for this redox-induced movement of Fe1 implied by these results provides further support for our proposed mechanism of Rbr's hydrogen peroxide reductase activity (*4*), which requires rapid cycling (∼30 s^{-1}) (*17*) between diferrous and diferric diiron sites having the structures shown in Figure 1 for Rbr_{red} and Rbr_{ox}, respectively. ZnS_4Rbr does not show peroxidase activity, presumably because the [$Zn(SCys)_4$] site cannot mediate electron transfer to the diiron site. Thus, rereduction of the diferric site during peroxidase turnover of the all-iron Rbr most likely occurs by sequential one-electron transfer from the proximal [$Fe(SCys)_4$] site (cf. Figure 1), which implies transient formation of a mixed-valent diiron site. One or both of the diiron site structures in the cryo- reduced ZnS_4Rbr crystal is (are) likely to represent that (those) of transient mixed-valent diiron site(s) that must occur upon return of the diferric to the diferrous oxidation level during peroxidase turnover.

REFERENCES

1. LeGall, J., Prickril, B. C., Moura, I., Xavier, A. V., Moura, J. J. G., and Huynh, B. M. (1988) Isolation and characterization of rubrerythrin, a non-heme iron protein from *Desulfovibrio vulgaris* that contains rubredoxin centers and a hemerythrin-like binuclear iron cluster, *Biochemistry 27*, 1636−1642.
2. deMaré, F., Kurtz, D. M., Jr., and Nordlund, P. (1996) The structure of *Desulfovibrio vulgaris* rubrerythrin reveals a unique combination of rubredoxin-like FeS_4 and ferritin-like diiron domains, *Nat. Struct. Biol. 3*, 539−546.
3. Sayle, R., and Milner-White, E. J. (1995) RASMOL—biomolecular graphics for all, *Trends Biochem. Sci. 20*, 374−376.
4. Jin, S., Kurtz, D. M., Jr., Liu, Z.-J., Rose, J., and Wang, B.-C. (2002) X-ray crystal structures of reduced rubrerythrin and its azide adduct: a structure-based mechanism for a non-heme diiron peroxidase, *J. Am. Chem. Soc. 124*, 9845−9855.
5. Kurtz, D. M., Jr., and Prickril, B. C. (1991) Intrapeptide sequence homology in rubrerythrin from *Desulfovibrio vulgaris*. Identification of potential ligands to the diiron site, *Biochem. Biophys. Res. Commun. 181*, 337−341.
6. Gupta, N., Bonomi, F., Kurtz, D. M., Jr., Ravi, N., Wang, D. L., and Huynh, B. H. (1995) Recombinant *Desulfovibrio vulgaris* rubrerythrin. Isolation and characterization of the diiron domain, *Biochemistry 34*, 3310−3318.
7. Smoukov, S. K., Davydov, R. M., Doan, P. E., Sturgeon, B., Kung, I. Y., Hoffman, B. M., and Kurtz, D. M., Jr. (2003) EPR and ENDOR evidence for a 1-His, hydroxo-bridged mixed-valent diiron site in *Desulfovibrio vulgaris* rubrerythrin, *Biochemistry 42*, 6201−6208.
8. Sieker, L. C., Holmes, M., Le Trong, I., Turley, S., Santarsiero, B. D., Liu, M. Y., LeGall, J., and Stenkamp, R. E. (1999) Alternative metal-binding sites in rubrerythrin (comment), *Nat. Struct. Biol. 6*, 308−309.
9. Sieker, L. C., Holmes, M., Le Trong, I., Turley, S., Liu, M.-Y., LeGall, J., and Stenkamp, R. E. (2000) The 1.9 Å crystal structure

of "as isolated" rubrerythrin from *Desulfovibrio vulgaris*: some surprising results, *J. Biol. Inorg. Chem. 5*, 505−513.
10. Li, M., Liu, M.-Y., LeGall, J., Gui, L. L., Liao, J., Jiang, T., Zhang, J.-P., Liang, D.-C., and Chang, W.-R. (2003) Crystal structure studies on rubrerythrin: enzymatic activity in relation to the zinc movement, *J. Biol. Inorg. Chem. 8*, 149−155.
11. Bonomi, F., Kurtz, D. M., Jr., and Cui, X. (1996) Ferroxidase activity of recombinant *Desulfovibrio vulgaris* rubrerythrin, *J. Biol. Inorg. Chem. 1*, 67−72.
12. Pierik, A. J., Wolbert, R. B. G., Portier, G. L., Verhagen, M. F. J. M., and Hagen, W. R. (1993) Nigerythrin and rubrerythrin from *Desulfovibrio vulgaris* each contain two mononuclear iron centers and two dinuclear iron clusters, *Eur. J. Biochem. 212*, 237−245.
13. Lumppio, H. L., Shenvi, N. V., Summers, A. O., Voordouw, G., and Kurtz, D. M., Jr. (2001) Rubrerythrin and rubredoxin oxidoreductase in *Desulfovibrio vulgaris*. A novel oxidative stress protection system, *J. Bacteriol. 183*, 101−108.
14. Liu, M.-Y., and LeGall, J. (1990) Purification and characterization of two proteins with inorganic pyrophosphatase activity from *Desulfovibrio vulgaris*: Rubrerythrin and a new, highly active enzyme, *Biochem. Biophys. Res. Commun. 171*, 316−318.
15. Coulter, E. D., Shenvi, N. V., and Kurtz, D. M., Jr. (1999) NADH peroxidase activity of rubrerythrin, *Biochem. Biophys. Res. Commun. 255*, 317−323.
16. Coulter, E. D., Shenvi, N. V., Beharry, Z., Smith, J. J., Prickril, B. C., and Kurtz, D. M., Jr. (2000) Rubrerythrin-catalyzed substrate oxidation by dioxygen and hydrogen peroxide, *Inorg. Chim. Acta 297*, 231−234.
17. Coulter, E. D., and Kurtz, D. M., Jr. (2001) A role for rubredoxin in oxidative stress protection in *Desulfovibrio vulgaris*: catalytic electron transfer to rubrerythrin and two-iron superoxide reductase, *Arch. Biochem. Biophys. 394*, 76−86.
18. Jenney, F. E., Jr., Verhagen, M. F. J. M., Cui, X., and Adams, M. W. W. (1999) Anaerobic microbes: oxygen detoxification without superoxide dismutase, *Science 286*, 306−309.
19. Alban, P. S., Popham, D. L., Rippere, K. E., and Krieg, N. R. (1998) Identification of a gene for a rubrerythrin/nigerythrin-like protein from *Sprillum volutans* by using amino acid sequence data from mass spectrometry and NH_2-terminal sequencing, *J. Appl. Microbiol. 85*, 875−882.
20. Alban, P. S., and Krieg, N. R. (1998) A hydrogen peroxide resistant mutant of *Spirillum volutans* has NADH peroxidase activity but no increased oxygen tolerance, *Can. J. Microbiol. 44*, 87−91.
21. Sztukowska, M., Bugno, M., Potempa, J., Travis, J., and Kurtz, D. M., Jr. (2002) Role of rubrerythrin in the oxidative stress response of *Porphyromonas gingivalis*, *Mol. Microbiol. 44*, 479−488.
22. Otwinowski, Z. (1993) in *Proceedings of the CCP4 weekend* (Sawyer, L., Isaacs, N., and Bailey, S., Eds.) pp 56−62, Daresbury Laboratories, Warrington, U.K.
23. Glusker, J. P., Lewis, M., and Rossi, M. (1994) *Crystal structure analysis for chemists and biologists*, VCH Publishers, New York.
24. Strahs, G., and Kraut, J. (1968) Low-resolution electron-density and anomalous-scattering-density maps of *Chromatium* high-potential iron protein, *J. Mol. Biol. 35*, 503−512.
25. http://www.bmsc.washington.edu/scatter/.
26. Brünger, A. T., Adams, P. D., Clore, G. M., DeLano, W. L., Gros, P., Grosse-Kunstleve, R. W., Jiang, J. S., Kuszewski, J., Nilges, M., Pannu, N. S., Read, R. J., Rice, L. M., Simonson, T., and Warren, G. L. (1998) Crystallography & NMR system: A new software suite for macromolecular structure determination, *Acta Crystallogr, Sect. D: Biol. Crystallogr. 54*, 905−921.
27. Jones, T., Zou, J., Cowan, S., and Kjeldgaard, M. (1991) Improved methods for building protein models in electron density maps and the location of errors in these models, *Acta Crystallogr. A47*, 110−119.
28. Kurtz, D. M., Jr. (1990) Oxo- and hydroxo-bridged diiron complexes: A chemical perspective on a biological unit, *Chem. Rev. 90*, 585−606.
29. Solomon, E. I., Tuczek, F., Root, D. E., and Brown, C. A. (1994) Spectroscopy of binuclear dioxygen complexes, *Chem. Rev. 94*, 827−856.
30. Solomon, E. I., Brunold, T. C., Davis, M. I., Kemsley, J. N., Lee, S.-K., Lehnert, N., Neese, F., Skulan, A. J., Yang, Y.-S., and Zhou, J. (2000) Geometric and Electronic Structure/Function Correlations in Non-Heme Iron Enzymes, *Chem. Rev. 100*, 235−349.
31. Dave, B. C., Czernuszewicz, R. S., Prickril, B. C., and Kurtz, D. M., Jr. (1994) Resonance Raman spectroscopic evidence for the FeS_4 and Fe−O−Fe sites in rubrerythrin from *Desulfovibrio vulgaris*, *Biochemistry 33*, 3572−3576.
32. Jin, S. (2002) Ph.D. Thesis, Department of Chemistry, University of Georgia, Athens, GA.
33. Laskowski, R. A., Macarthur, M. W., Moss, D. S., and Thornton, J. M. (1993) Procheck—a program to check the stereochemical quality of protein structures, *J. Appl. Crystallogr. 26*, 283−291.
34. Dauter, Z., Wilson, K. S., Sieker, L. C., Moulis, J. M., and Meyer, J. (1996) Zinc- and iron-rubredoxins from *Clostridium pasteurianum* at atomic resolution: a high-precision model of a ZnS_4 coordination unit in a protein, *Proc. Natl. Acad. Sci. U.S.A. 93*, 8836−8840.
35. Jin, S., Kurtz, D. M., Jr., Liu, Z.-J., Rose, J., and Wang, B.-C. (2004) Displacement of iron by zinc at the diiron site of *Desulfovibrio vulgaris* rubrerythrin. X-ray crystal structure and anomalous scattering analysis, *J. Inorg. Biochem.* (in press).
36. DeWitt, J. G., Bentsen, J. G., Rosenzweig, A. C., Hedman, B., Green, J., Pilkington, S., Papaefthymiou, G. C., Dalton, H., Hodgson, K. O., and Lippard, S. J. (1991) X-ray absorption, Mössbauer, and EPR studies of the dinuclear iron center in the hydroxylase component of methane monooxygenase, *J. Am. Chem. Soc. 113*, 9219−9235.
37. Eriksson, M., Jordan, A., and Eklund, H. (1998) Structure of *Salmonella typhimurium* nrdF ribonucleotide reductase in its oxidized and reduced forms, *Biochemistry 37*, 13359−13369.
38. Logan, D. T., Su, X. D., Aberg, A., Regnstrom, K., Hajdu, J., Eklund, H., and Nordlund, P. (1996) Crystal structure of reduced protein R2 of ribonucleotide reductase: the structural basis for oxygen activation at a dinuclear iron site, *Structure 4*, 1053−1064.
39. Lindqvist, Y., Huang, W., Schneider, G., and Shanklin, J. (1996) Crystal structure of delta9 stearoyl-acyl carrier protein desaturase from castor seed and its relationship to other di-iron proteins, *EMBO J. 15*, 4081−4092.
40. Moche, M., Shanklin, J., Ghoshal, A., and Lindqvist, Y. (2003) Azide and acetate complexes plus two iron-depleted crystal structures of the di-iron enzyme delta9 stearoyl-acyl carrier protein desaturase. Implications for oxygen activation and catalytic intermediates, *J. Biol. Chem. 278*, 25072−25080.
41. Whittington, D. A., and Lippard, S. J. (2001) Crystal structures of the soluble methane monooxygenase hydroxylase from *Methylococcus capsulatus* (Bath) demonstrating geometrical variability at the dinuclear iron active site, *J. Am. Chem. Soc. 123*, 827−838.
42. Day, E. P., David, S. S., Peterson, J., Dunham, W. R., Bonvoisin, J. J., Sands, R. H., and Que, L., Jr. (1988) Magnetization and electron paramagnetic resonance studies of reduced uteroferrin and its "EPR-silent" phosphate complex, *J. Biol. Chem. 263*, 15561−15567.

BI0356193